RESEARCH ARTICLE

VOLCANICA

Pit crater formation and caldera subsidence at Puyehue-Cordón Caulle (Chile) documented with satellite, drone, and field observations

Alonzo Olitt[α,β], Diego Lobos-Lillo[α], Matthew E. Pritchard *[α], Carolina Muñoz-Saez[α], Patrick Phelps[γ], and Philipp Ruprecht[δ]

[α] Department of Earth and Atmospheric Sciences, Cornell University, Ithaca, New York, USA.
[β] Now at: Department of Earth, Planetary, and Space Sciences, University of California, Los Angeles, Los Angeles, California, USA.
[γ] Department of Geological Sciences, California State University, Fullerton, California, USA.
[δ] Department of Geological Sciences and Engineering, University of Nevada, Reno, Nevada, USA.

Submitted: 2025-06-15 | Accepted: 2026-06-22 | Published: 2026-07-02

Editor: E.M. Paguican | Production: G. Seropian

Abstract

Pit craters are observed throughout the solar system, but are rarely seen forming. Here we document pit crater formation and characteristics following the 2011–2012 Cordón Caulle rhyolitic eruption using satellite and drone data with field observations. Syn-eruptive shallow intrusion (laccolith) uplift and subsequent subsidence at Cordón Caulle are found to be responsible for the creation of faults and fractures as well as at least 349 collapse pits. At Puyehue volcano, we measure nearly 35 m of subsidence within the 2.5 km wide summit caldera from 2016–2024 using digital elevation models leading to ring fractures and pit craters forming inside the caldera. Some pit craters may form from melting snow buried by tephra deposited during 2011–2012. This study offers a unique example of near real-time pit crater formation and evolution, which may be applied to better understanding these processes on Earth and other planetary bodies.

Keywords: Volcano; Pit; Crater; Puyehue; Cordon Caulle; Laccolith.

1 Introduction

Pit craters are ubiquitous geologic features that have been observed on every terrestrial planet in our solar system, as well as on asteroids and moons [e.g. Head III and Wilson 1993; Prockter et al. 2002; Whitten and Martin 2019]. They are semi-circular depressions that can take cylindrical, bowl or inverted conical shapes and are often found in volcanic regions [Okubo and Martel 1998; Ferrill et al. 2011]. Their appearance closely resembles that of impact craters; however, they lack raised rims or surrounding ejecta deposits [Wyrick et al. 2004]. Pit crater size can vary significantly from meter to kilometer scale in diameter, with those found on other planetary bodies such as Mars and Venus being the largest [Ferrill et al. 2004; Kling 2020]. Additionally, pit craters are commonly found grouped together in linear assemblages which are referred to as pit crater chains. Pit chains can often resemble features similar to troughs, where individual pits may or may not be visible based on how closely they formed and how much they have coalesced over time [Crumpler and Aubele 1978]. In Iceland, similar features are called sinkholes and have been observed forming in volcanic areas [Clifton and Einarsson 2005; Björnsdóttir and Einarsson 2013; Bufféral et al. 2023; Shevchenko et al. 2024; Hurley et al. 2025]. The term sinkhole does not require a circular shape and is usually related to karst and thermokarst, so is appropriate for the thermokarst features in Iceland [Shevchenko et al. 2024].

Despite being common features, the mechanisms responsible for pit crater formation are still debated [Kling 2020]. Currently, the literature on proposed mechanisms of pit crater formation falls into two main groups (Figure 1): (1) Explosive formation directly through magmatic eruptions or phreatomagmatic eruptions (hydro-volcanic explosions caused by residual heat from magma superheating groundwater) [Hughes et al. 2018]; and (2) collapse formation, where subterranean void space is formed from volcanic, thermokarst (melting subterranean snow or ice), or tectonic origin causing overlying material to drain into newly formed void spaces producing pit craters on the surface [Wyrick and Buczkowski 2022]. Recently, the collapse mechanism has emerged as the leading explanation for pit crater formation with support from numerous examples on Mars [Wyrick et al. 2004], Venus [Kling 2020], Earth [Ferrill et al. 2011] and in sandbox experiments [Ferrill et al. 2004].

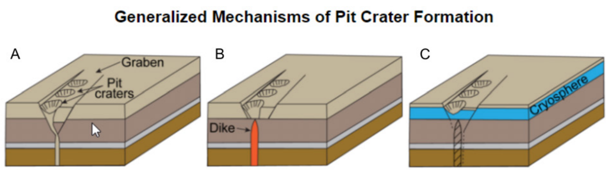

Figure 1: Cartoon of pit crater formation mechanisms from Kling [2020] and adapted from Wyrick et al. [2004]. [A] Collapse formation where overlying material drains into void space created by extensional faulting. [B] Explosive formation caused by dike intrusion. [C] Explosive or collapse formation where faults or dikes come into contact with the hydrosphere.

Previous studies of pit craters on other planetary bodies have relied mainly on analyzing pit crater morphology measured using satellite imagery to interpret how pits have formed [e.g. Wyrick et al. 2004; Wyrick and Buczkowski 2022] . However, more recent findings have suggested that morphometric characteristics alone are not diagnostic of how pit craters formed [Kling and Byrne 2022; Magee et al. 2022]. Thus, stud-

* pritchard@cornell.edu

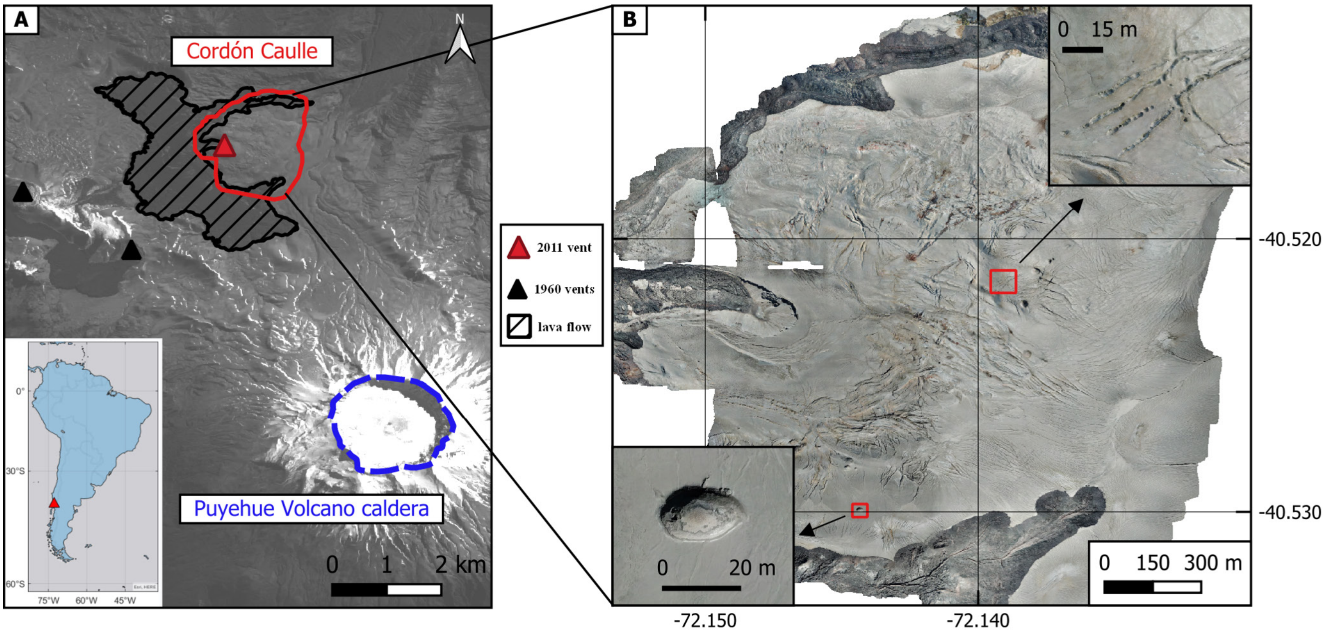

Figure 2: [A] Landsat 9 image from April 2022 encompassing a portion of the PCC volcanic complex. Red triangle is the vent of the 2011–2012 Cordón Caulle eruption, while the red outline is the spatial extent of the high spatial resolution drone image shown in panel B. Blue dashed lines define the extent of the Puyehue volcano caldera. The inset shows a map of South America where the red triangle marks the location of the PCC volcanic complex. [B] High resolution (10 cm px^{-1}) drone optical image acquired in March 2022 encompassing the Cordón Caulle shallow intrusion area. Insets show characteristic pit craters with locations defined by red boxes on the map. Bottom left inset shows an isolated circular-shaped pit crater and the top right inset shows multiple pit chains consisting of small individual pits oriented in a linear pattern.

ies of pit craters found on Earth where we can incorporate ground observations (including seismic reflection observations [Magee et al. 2022; Pryce et al. 2025; Somoza et al. 2025]) along with high resolution remote sensing data are especially important for understanding how pit craters form and evolve.

Unfortunately, the occurrence of pit crater formation on Earth is relatively infrequent and often obscured by active erosional processes affecting pit crater morphology on relatively short timescales compared to other planetary pits. Previously, there have been a few other examples of active pit crater formation documented on Earth in volcanic areas: at several locations in Iceland (where they are called sinkholes as mentioned above) [Ferrill et al. 2011; Shevchenko et al. 2024; Hurley et al. 2025], and at Kīlauea, Hawaiʻi in 2018 [Kling 2020]. Here we present an example from a different setting (volcanic arc) following the 2011–2012 Cordón Caulle eruption that occurred within the Puyehue-Cordón Caulle (PCC) volcanic complex. The availability of high spatial and temporal resolution remote sensing data of the PCC region spanning all the way prior to the 2011–2012 eruption and subsequent pit crater formation at two separate locations in the PCC complex, makes this a good opportunity to study pit crater formation while it is happening and with great detail. As a result, this study of pit crater formation offers a unique insight into the mechanisms responsible for widespread pit crater formation and evolution in the carapace above a newly formed shallow intrusion (called a laccolith by Castro et al. [2016]) and within an actively subsiding caldera which may be applicable to other locations with similar geologic environments. We use the term pit crater instead of sinkhole at PCC because all of the features are quasi-circular, and the relation to thermokarst is not certain, although there was snow buried by 2011–2012 eruption tephra [Pistolesi et al. 2015] that could play a role in their formation.

1.1 Puyehue-Cordón Caulle (PCC) volcanic complex

The PCC volcanic complex is located within the Andean Southern Volcanic Zone (SVZ) in Chile (Figure 2). It consists of the Cordón Caulle fissure system, which is defined by multiple volcanic edifices within a large NW–SE oriented graben, and Puyehue volcano [Singer et al. 2008]. Cordón Caulle lies in the northwest portion of the complex and has had three historical eruptions over the last 100 years, while Puyehue is a stratovolcano located to the southeast of Cordón Caulle which hasn't erupted for about ~1000 years [Singer et al. 2008].

1.2 2011–2012 Cordón Caulle eruption

The most recent eruption within the PCC complex was the 2011–2012 Cordón Caulle eruption, which was primarily rhyolitic and characterized by multiple distinct eruptive and effusive phases as well as syn-eruptive shallow intrusion emplacement [Castro et al. 2016]. The eruption began on June 4, 2011 with a sub-Plinian explosive phase that transitioned into a hybrid phase after June 15, 2011 that lasted until March, 2012 [Bonadonna et al. 2015]. In total, ~1.0 km^3 dense rock equivalent (DRE) of rhyolite tephra and lava was expelled during the eruption [Naranjo et al. 2017; Delgado et al. 2019] in addition to the shallow intrusion of a ~0.455 km^3 [Castro et al. 2016;

Lillo et al. 2024]. Syn-eruptive shallow intrusion emplacement occurred during the first month of the eruption and resulted in nearly 250 m of surface uplift during that period [Castro et al. 2016]. In response, deformation features in the form of pit craters and fractures occurred on the carapace above the shallow intrusion (called a forced fold by Magee [2024]). While the development of fractures has been noted in previous studies [Castro et al. 2016; Magee 2024], this study presents the first description of the pit craters. Here we focus specifically on pit craters forming on the forced fold and within Puyehue caldera, as we did not find any evidence of pit craters on the lava flow from remote sensing data or during field seasons, though other studies [De Crescenzo et al. 2022; Bersson et al. 2026] have shown examples of pit crater formation in basaltic to rhyolitic lava flows.

1.3 Puyehue volcano

Approximately 6 km southeast from the site of the 2011–2012 Cordón Caulle eruption lies Puyehue volcano, a stratovolcano with a 2.5 km wide and ~300 m deep summit caldera (shown in Figure 2). The modern Puyehue volcano was built over the last 69 kyr and has had diverse eruptive products ranging from basaltic to rhyolitic lavas [Singer et al. 2008]. The most recent set of eruptions at ~1 ka are responsible for forming the current summit caldera [Singer et al. 2008]. Activity at Puyehue was noted during the 2011–2012 eruption where inferred magma withdrawal from a reservoir located beneath Puyehue volcano partially fed the eruption [Jay et al. 2014]. The draining of magma from this reservoir (along with another to the north of the 2011–2012 eruption site) resulted in subsidence of ~25 cm that was measured through the use of Interferometric Synthetic Aperture Radar (InSAR). To our knowledge, no other previous studies have reported any significant change in activity or the appearance of surface deformation at Puyehue following the 2011–2012 eruption.

Using high spatial resolution satellite datasets, we show significant post-eruptive deformation within Puyehue caldera, evidenced by the appearance of concentric ring fractures and pit craters along the caldera floor. The timing associated with the appearance of these features is of particular interest as caldera deformation is commonly closely tied to periods of eruption [De Natale et al. 1997], yet Puyehue volcano has not erupted in over 1 kyr [Global Volcanism Program 2025]. Thus, evidence of active deformation could be signalling some form of new or increased activity within the system. Deciphering whether this activity is directly related to the 2011–2012 Cordón Caulle eruption or rather an independent sign of unrest at Puyehue was therefore also a focus of this study. By looking into the timing and evolution of pit craters and ring fractures inside Puyehue caldera using remote sensing data we sought to provide some insight into the responsible processes and any possible future hazard related to current deformation.

1.4 Pit crater formation mechanisms

Within the collapse formation framework for the formation of pit craters (Figure 1), dike intrusions [Scott et al. 2002], dilational faulting [Wyrick et al. 2004; Ferrill et al. 2011; Whitten and Martin 2019], and melting of buried snow or ice [Shevchenko et al. 2024] have been proposed as mechanisms in which subterranean void space can be created allowing for the formation of pit craters. Sinkholes have been suggested to form above snow buried by the Askja, Iceland 1875 eruption tephra [Shevchenko et al. 2024; Shoemaker Thackston et al. 2024]. The 2011–2012 eruption of PCC occurred during the winter when up to several meters of snow were covering the ground (especially on Puyehue) as seen in photographs and satellite images (Figure 6B) as well as interspersed with the tephra [Pistolesi et al. 2015]. Modelling from Wyrick and Smart [2009] has shown that dike intrusions without dilatational faults likely do not result in the formation of pit crater chains. On the other hand, modelling of dilational faulting has shown that formation of individual pits, pit crater chains and various pit crater morphology (i.e. cylindrical, conical, bowl, troughs) are all possible results when occurring in unconsolidated material [Wyrick and Smart 2009; Holohan et al. 2011; Smart et al. 2011; Poppe et al. 2015; Hardy 2021]. Indeed, the upper several tens of meters of the forced fold at Cordón Caulle is made of unconsolidated tephra [Lillo et al. 2024].

2 Methods and data

We use multiple satellite datasets as well as UAV (unmanned aerial vehicle, also known as a drone) imagery, field photographs and in-situ measurements made during recent fieldwork campaigns. Our satellite data include synthetic aperture radar (SAR) imagery from Capella and high spatial resolution (<3 m $pixel^{-1}$) optical imagery collected from GeoEye-1 (GE1), Worldview-1 (WV1), Worldview-2 (WV2), Worldview-3 (WV3), PlanetScope, and Pléiades satellites (Table 1). In addition to optical imagery, we also collect digital elevations models (DEMs) generated from SAR and optical imagery used in previous studies of post-eruptive deformation at PCC from Delgado et al. [2016] and Lillo et al. [2024] as well as a newly acquired Pléiades stero-optical DEM. The UAV remote sensing data included an orthorectified optical image, DEM, and thermal map of the shallow intrusion area acquired in March 2022 (though only the drone optical image and DEM are utilized during our analysis and is included as part of the data published with this study). Satellite optical images are mainly used for analyzing the timing and evolution of pit craters, fractures, and other notable features while the drone data are only available at Cordón Caulle and used for identifying and obtaining morphometric properties of visible pit craters. The higher spatial resolution of the drone data is crucial for identifying smaller pits and making accurate morphological measurements, but based on field observations we know that some craters are missed. For reference, the drone has a spatial resolution of 10 cm px^{-1} while the highest resolution satellite images are only able to achieve ~50 cm px^{-1}.

For all optical satellite images (except for PlanetScope images) both a panchromatic (greyscale) and multispectral (RGB) image are available, but only the panchromatic images are used for analysis due to the increased spatial resolution compared to their multispectral counterparts. The spatial resolution of panchromatic imagery is 0.46 m px^{-1} compared to 1.8 m px^{-1} for multispectral at nadir for GE1, WV1, WV2 and 0.31 m px^{-1} compared to 1.24 m px^{-1} at nadir for WV3. For

Table 1: High spatial resolution remote sensing datasets used to study pit crater formation and evolution at PCC. Satellite data from Vantor, Planet, and Capella was provided through NASA's Commercial SmallSat Data Acquisition (CSDA) Program while Pléiades data was acquired thanks to the French national space agency Centre National d'Études Spatiales (CNES). UAV data are reported here for the first time.

Satellite/Platform	Spatial Resolution	Mean Temporal Resolution	Dates	Source
GeoEye-1	50 cm px^{-1}	8.3 days	2011–Pres	Vantor
Worldview-1	50 cm px^{-1}	5.9 days	2011–Pres	Vantor
Worldview-2	50 cm px^{-1}	3.7 days	2011–Pres	Vantor
Worldview-3	31 cm px^{-1}	4.5 days	2016–Pres	Vantor
PlanetScope	3 m px^{-1}	~1 day	2016–2023	Planet
Pléiades	50 cm px^{-1}	26 days	2014, 2024	CNES/Airbus
UAV	10 cm px^{-1}	N/A	2022	Rice/Cornell
Capella	30 cm px^{-1}	2–5 hours	2024	Capella Space

Pléiades images, the spatial resolution of panchromatic images is 0.5 m px^{-1} compared to 2 m px^{-1} for multispectral images. Many of the pits we map using the high-resolution drone data have diameters on the scale of 1 m, therefore using the higher spatial resolution panchromatic images significantly increases our ability to identify as many pit craters as possible from the satellite data.

2.1 Field work

The field work component of this study consisted of collecting very high spatial resolution remote sensing data using a UAV as well as taking photographs of individual features (pit craters and fractures) on the forced fold over multiple field seasons to support remote sensing analysis. Initial observations of the physical characteristics of PCC pit craters, faults, and fractures was done primarily by analyzing remote sensing data from the UAV and by satellite while field work done during January 2025 was carried out to provide confirmation of these observations and measurements. Field photos were taken primarily using cell phone cameras as well as with drones when possible. Most photographs of Cordón Caulle pit craters were taken on the south and southeast sides of the forced fold, as access to pits on the north side was slightly more difficult due to the terrain and increased distance from our campsite. Photos of Puyehue pit craters were not able to be taken due to persistent snow cover within the caldera during our visit in January 2025 (though circular melt features were present as shown in Supplementary Material 1 Figure S1). The total number of pit craters (>300 on the forced fold) as well as having a high-resolution drone image over the whole forced fold meant that we did not prioritize photographing each individual pit during the field seasons. Instead, an effort was made to obtain photographs documenting the different pit crater morphologies present (e.g. cylindrical, conical or bowl shaped), in addition to any very small or shallow pits likely obscured in the remote sensing imagery. Also, a single field measurement of pit crater diameter was made using a hand-held laser rangefinder to roughly compare the accuracy with our measurements made using drone remote sensing data. The diameter of the pit crater measured in the field yielded a result within 1.2 % of the measured value from the drone data (see Supplementary Material 1 Table S1). A corresponding accuracy assessment of pit crater depth measurements was not included since snow was still filling the measured pit crater during the time of our field measurement.

2.2 Collection and processing of drone data

The drone data was collected from March 14 to March 25, 2022, utilizing a UAV for optical imaging. The DJI Mavic Pro Platinum, equipped with a camera resolution of 4000 × 3000 px, was employed for optical data collection. To minimize shadows in the imagery, optical data collection took place when the sun was near its zenith, typically between 1:00 pm and 4:00 pm local time. The methodology involved installing 1×1 m reflectors as ground control points (roughly corresponding to ~10×10 px in the orthophoto) daily and surveying their location with a handheld Global Positioning System receiver. In terms of data yield, the optical drone captured 5,021 images at an altitude of 118 m, with a coverage area of 3.79 km^2 and a ground resolution of 4.32 cm px^{-1}. The optical data had a reprojection error of 2.55 px, which represents the average pixel deviation between the projected and actual position of tie points identified across multiple images. The average camera location error was 14.21 m total, comprising a horizontal error in the E–W direction of 2.73 m, horizontal error in the N–S direction of 2.62 m, and vertical error of 13.70 m. This spatial uncertainty primarily reflects the positional accuracy limitations of the onboard GPS in the drone rather than issues with the photogrammetric reconstruction itself. The final ortho-mosaic was exported with a spatial resolution of 10 cm px^{-1}.

The optical digital elevation model (DEM) was generated from a dense point cloud with a calculated point density of 8.37 points m^{-2} and a resolution of 34.6 cm px^{-1}. Interpolation was applied during processing to fill gaps in the point cloud data. The final DEM covers an elevation range from approximately 1.22 km to 1.67 km above sea level. An accuracy assessment of the drone DEM to establish its suitability for measuring pit crater morphometric properties was conducted by comparing against a satellite based DEM. The results of Supplementary Material 1 Figure S2 show that the drone and satellite DEM produce similar estimates of pit crater morphology for multiple pits across the forced fold. This, along with the dense point cloud distribution and consistent processing parameters, suggest the drone DEM contains reliable terrain representations suitable for the analytical purposes of this study.

The UAV data was processed using `AGISOFT Metashape Pro` (version 1.8.2). The photogrammetric workflow followed standard structure-from-motion procedures involving photo alignment, dense point cloud generation, mesh creation, and texture building. The optical data processing produced a sparse point cloud of 1,714,903 tie points and a dense cloud containing 44,861,747 points, which was transformed into a mesh with 7,460,018 faces. The final ortho-mosaic and DEM are in the WGS 84 (EPSG:4326) coordinate system.

2.3 DEM generation and coregistraion

A total of 22 PCC satellite DEMs generated by Delgado et al. [2016] and Lillo et al. [2024] spanning from 2011–2019 are available, all of which covered both the shallow intrusion area and Puyehue volcano (see Lillo et al. [2024] for full list of DEM dates). Additionally, we created a DEM with more recent Pléiades optical satellite imagery from March 2024. The tri-stereo acquisitions of Pléiades imagery allow for the use of photogrammetry techniques to extract surface elevation data from the optical images. We use the open-source `MicMac` software developed by the French National Institute of Geographic and Forestry Information (IGN). Through exploiting the different viewing geometries provided by collecting two or three separate images during a single acquisition (stereo or tri-stereo imagery), `MicMac` produces a single orthorectified image and DEM, both of which are used in our analysis.

The raw 2024 Pléiades DEM generated using `MicMac` contain a significant horizontal and vertical offset compared to the other DEMs used in this study. Thus, to properly compare the new DEM with previous data, we correct for the offset by coregistering it with a reference DEM from April 2014 that is also produced using Pléiades optical imagery [Lillo et al. 2024]. Given its similar origin, the decision to use this as the reference DEM in the coregistration process was made in an effort to reduce any errors and offset remaining after coregistration. To stay consistent with how earlier PCC DEMs from Lillo et al. [2024] were coregistered, we use the Enhanced Co-registration and Bias Correction (ECBC) method developed by Nuth and Kääb [2011] while masking out Puyehue caldera and the 2011–2012 eruption region (areas of deformation) to coregister the new 2024 DEM to the 2014 DEM. A further description of how this method works and why it was chosen can be found in Lillo et al. [2024]. For reference, the final coregistration shifted the new Pléiades DEM from March 2024 by 39 m horizontally and 2 m vertically.

3 Results

3.1 Pit crater formation on Cordón Caulle forced fold

3.1.1 *Mapping and measuring pit crater morphometric properties: Drone data analysis*

Our high spatial resolution drone data from March 2022 served as a baseline for identifying and mapping pit craters on the forced fold. A total of 349 individual pit craters are identified and mapped in addition to 26 pit crater chains. We also mapped the most prominent faults and fractures visible at the surface (totaling 60), though a much greater number of faults with no or subtle surface trace likely exist. Figure 3 shows the results of these mapped features overlaid on top of the drone optical image. The spatial distribution of pit craters is not localized to any single area, but rather widely distributed over the entire extent of the forced fold. Large pits mainly occur further away from the vent while smaller pits occur both close and far. Not very many pits (<10 %) show up in the large fracture swarms to the east of the vent, likely since the degree of deformation overshadows any pit formation. Pit crater chains can be found to the south of the vent, towards the base of the tephra cone that was formed during the initial explosive phase of eruption [Schipper et al. 2013], as well as to the northeast of the vent.

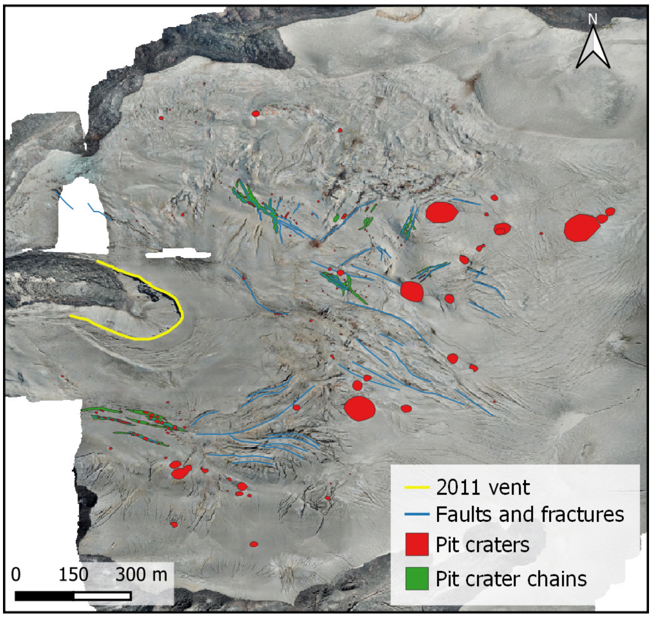

Figure 3: Cordón Caulle optical drone image from March 2022 with mapped pit craters (red), pit crater chains (green), and some of the larger fractures (blue). See the Data Availability statement to where to access the shapefiles and drone images used to make this figure. Deformation features are distributed in a horseshoe pattern around the vent (yellow) with large fractures being concentrated towards the south and east. Pit crater chains primarily show up to south and northeast of the vent and often coincide with similarly oriented faults. Pit craters are located all throughout the forced fold with the largest pit craters occurring closer towards the edges of the shallow intrusion.

In addition to mapping, morphological measurements are made utilizing spatial analysis tools within QGIS (an open-source geographical information system) to determine properties such as pit crater diameter, depth, area, volume and major-axis orientation (a detailed outline of the methodology used to map and measure pit craters can be found in Supplementary Material 1 Section 1). The measured depths of pit craters ranged from less than 1 meter to 33 meters and the diameter ranged from 1 to 100 meters (see the Data Availability Statement for the full database of Cordón Caulle pit crater morphometric properties) and the depths, diameters, and their ratios are plotted in Figure 4 and the ratio is fit with a lognormal distribution.

3.1.2 *Pit crater morphology comparisons*

We compare Cordón Caulle pit craters to pits found on Venus, Mars, Earth, and Mercury (Figure 4). While pit craters are also found on other bodies such as Eros and Phobos, we do not include many of these pits in our comparison since very limited or no morphometric measurements are available due to low resolution data or no DEMs [Veverka et al. 1994; Prockter et al. 2002]. The depth and diameter range of the Cordón Caulle pit craters overlaps with similar features in Iceland [Ferrill et al. 2011; Whitten and Martin 2019], Hawai'i [Okubo and Martel 1998; Kling 2020], and Syria [Frumkin and Naor 2019]. Across all pits, the depth to diameter ratio varies between 0.09 to 0.64 for pit craters and is not thought to be diagnostic of the formation mechanisms [Magee et al. 2022]. For what it is worth, the mean depth to diameter ratio of Cordón Caulle pit craters (0.31) is most similar to that of pits found at Nyx Mons, Venus (0.27) (Figure 4). Nyx Mons is a volcano located in the Bell Regio region of Venus with pit craters (mostly forming pit chains) and graben occurring along its flank where pits are believed to have formed through a collapse mechanism associated with faults formed from extensional stresses caused by the inflation of a magma chamber [Kling 2020].

3.1.3 *Comparing pit craters with tectonic features*

Mapping pit craters and faults on the forced fold reveals a clear association among the orientation of pit crater chains with the largest faults and graben observed in the drone data (Figure 3). Previous studies have shown that pit craters formed as a result of faulting tend to exhibit elongation in the same direction as the strike angle of the associated faults [Ferrill et al. 2004]. Thus, to establish a more quantitative correlation between these features, we use a rose diagram to plot the orientation of each pit crater's major-axis (axis along which pit craters are elongated) to compare with the orientation of fractures and faults (Figure 5). The results show that the predominant orientation of both pit craters major-axis and faults is NW–SE, similar to the orientation of the larger graben bounding the entire PCC volcanic complex and analysis using satellite imagery from Magee [2024], although there is a larger spread of azimuths in Magee [2024]. A more detailed map based on field observations is in progress [Aron et al. 2025]. Looking specifically at pit craters which form pit chains ('Chain Pit Craters' in Figure 5) shows that these pits are also predominately oriented NW–SE as well as slightly NE–SW which mirrors the orientation of the Liquiñe-Ofqui Fault Zone (LOFZ), a transform fault that runs through the eastern part of the PCC complex [e.g. Singer et al. 2008]. Additionally, chain pit craters appear to be more preferentially elongated in the same direction as faults compared to isolated pits. Some pit craters lie within troughs bounded by faults/fractures, for example south and northeast of the eruptive vent (Figure 3). This suggests that especially for pit crater chains, the mechanism of formation is tied to the occurrence of normal faults and graben.

3.1.4 *Timing and evolution of pit crater formation: Optical satellite data analysis*

Pre-eruption satellite imagery of Cordón Caulle clearly shows that pit craters (and the forced fold) do not exist before June 4, 2011 when the 9-month eruption period began (Figure 6). Optical and SAR satellite images after June 4, 2011 capture the sub-Plinian explosive phase that characterized the beginning of the eruption [Jay et al. 2014; Castro et al. 2016]. During this period areas around the vent are largely covered in snow and the large ash-plume and we see no evidence of pit crater formation from any of the available satellite imagery during the first month of eruption. A cloud free image from July 3, 2011 shows a smaller ash plume being emitted with most of the region surrounding the vent clearly visible (Figure 6B). Note that significant surface deformation is now visible, attributed to shallow intrusion emplacement which occurred during the initial month of eruption [Castro et al. 2016]. To the south, east and north of the vent, large extensional fractures formed in response to uplift caused by the shallow intrusion, however, there are still no signs of any individual pit craters by this date.

The first snow- and cloud-free high spatial resolution satellite optical image after July 3, 2011 is on April 10, 2012 and has at least 92 visible pit craters on the flank of the recently formed tephra cone and within fractures (Figure 6C). The first evidence of pit chains can be found to the north of the vent, where some of these pit chains are made up of clearly distinguishable individual pits, while others are made up of pit craters that had already mostly coalesced together. Towards the edge of the laccolith, around ~500 m northeast of the vent, at least one larger isolated pit (not in a pit chain) can be found with a few smaller pits nearby.

After April 2012, the next available snow and cloud free image in the collection comes nearly a year later on February 3, 2013 (Figure 6D). In total, we map 142 pit craters in the February 2013 image, resulting in at least 50 newly visible pit craters since April 2012. Here, we acknowledge that differences in the conditions (e.g. time of day, cloud cover, viewing angle, resolution, etc.) between satellite acquisitions may play a part in how many pits are visible in any single image. However, the consistency between image conditions (see Supplementary Material 1 Table S2), primarily the similar spatial resolution in addition to the lack of dark shadows and cloud cover, builds confidence that newly visible pits can be mainly attributed to pit crater formation rather than an improvement in image quality. New pits can be seen below the smaller fracture system south of the vent and within and outside the large fractures to the east of the vent. Additionally, the lava flow to the south and north of the vent had clearly extended along with the formation of many new fractures on the forced fold, illustrating the dynamic environment post eruption.

The final image available in our time series of optical satellite images before encountering a large time gap with no snow or cloud free imagery was from April 22, 2014 (Figure 6E). We map more than 70 new pit craters after the 14-month period between our 2013 and 2014 images, resulting in a total of at least 215 pit craters. Steam can be seen coming from these newly established pit crater chains, possibly indicating an increase to subsurface permeability in younger pit chains

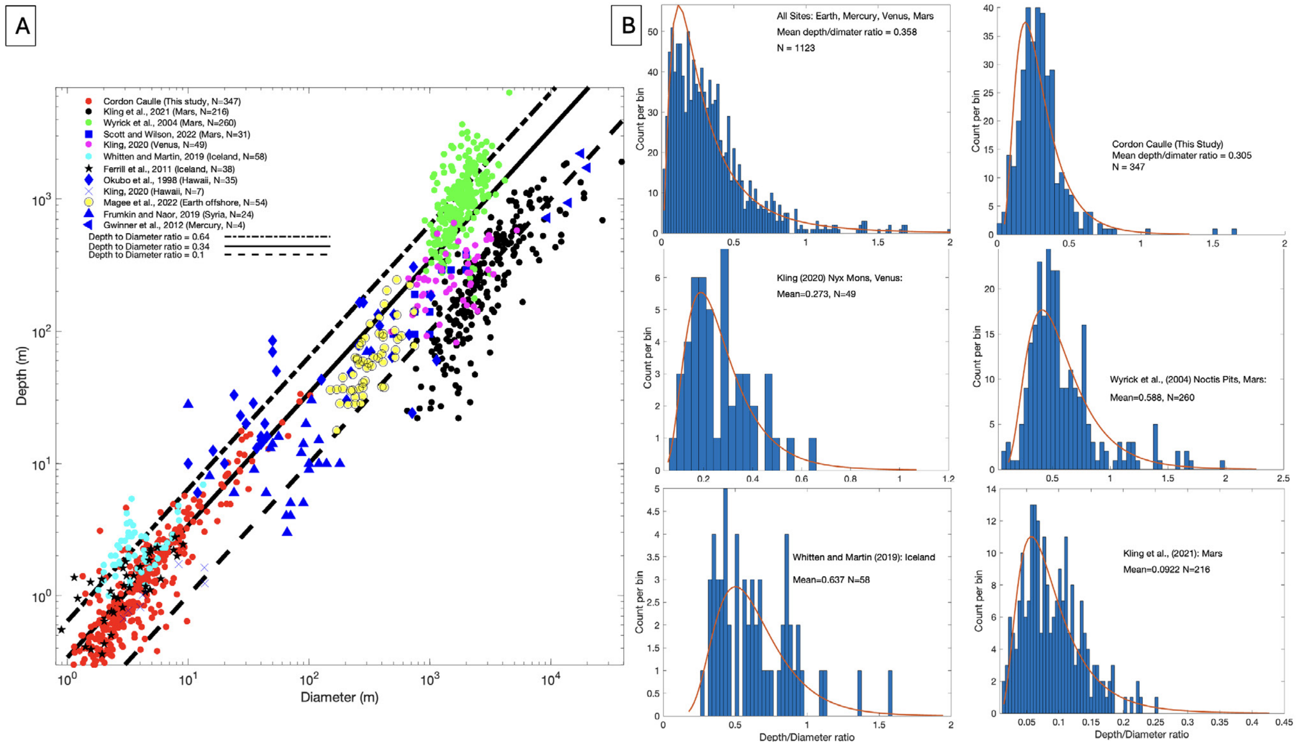

Figure 4: [A] Depth vs. diameter of 1123 pit craters compiled from Earth, Mercury, Venus, and Mars [Okubo and Martel 1998; Scott and Wilson 2002; Wyrick et al. 2004; Ferrill et al. 2011; Gwinner et al. 2012; Frumkin and Naor 2019; Whitten and Martin 2019; Kling 2020; Kling et al. 2021; Magee et al. 2022]. Lines represent different depth to diameter ratios, with 0.34 being the best fit for Cordón Caulle. [B] Histograms of depth/diameter ratios for selected regions in [A]. showing fit and mean values from lognormal probability density functions.

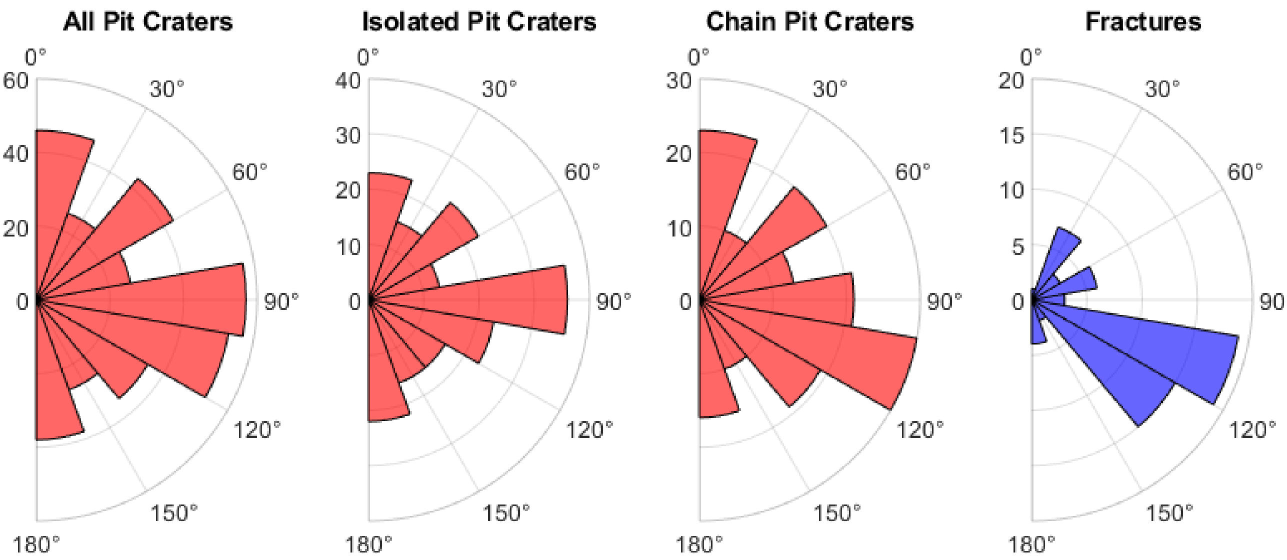

Figure 5: Rose diagrams comparing major axis orientations of different pit crater populations (all [n = 349], isolated [n = 235], pit crater chains [n = 26]) with large fracture and fault orientations [n = 64] from Figure 3.

compared to older pit chains. An alternative is that earlier pit craters also had steam but it was missed by the infrequent satellite images. New pits and existing pit crater growth can again be seen below the fractures directly to the south of the vent. Our mapping of visible pit craters suggests a possible increase in the frequency of pit crater formation from 2013–2014 compared to 2012–2013.

A comparison of pit craters mapped from the satellite images in 2014 and 2020 (Figure 6E, 6F) with pits mapped using the drone image from 2022 (Figure 3) reveals that a majority of the pits visible in 2022 had formed by 2014. Interestingly, some pit craters seen in the 2014 image cannot be seen in the 2020 and 2022 images, which suggests that subsequent deformation or erosional processes are significant enough to mask out a number of pit craters. Unfortunately, no snow and cloud free imagery was available from 2014 to 2020 in the datasets we used, so it is hard to constrain when or what caused some pits to disappear. On the other hand, part of the discrepancy between the total number of pits found in the 2014 image compared to the 2022 drone image can be attributed to the resolution of the imagery. Despite the WorldView optical imagery having a spatial resolution of 50 $cm\,px^{-1}$, pits with a diameter less than 3 meters are very difficult to discern.

3.1.5 *Pit crater morphology and field observations*

Pit crater morphology across the forced fold is quite variable with examples of conical, cylindrical and bowl-shaped pits throughout. Field photos provide detailed examples of the different pit crater morphologies present and show the different environments and layers with which pits formed (Figure 7). The plan view shape of pit craters is also extremely variable with almost anything in the continuum between perfectly circular to completely irregularly shaped being documented. However, even though there was great variability in terms of pit crater shape and size, we still consistently observed the characteristics diagnostic of collapse pits for every pit crater visited and photographed. Specifically, we found no evidence of any pit craters with raised rims, lava flows or ejecta surrounding the pit in a pattern suggesting an explosive origin. Pit crater photos also provide an insight into the variability of tephra layers deposited by the 2011–2012 eruption. Field pits with visible tephra layering in the pit walls are often more cylindrical shaped while layering within bowl-shaped pits was often masked by erosion of the top layer infilling the pit.

3.2 Puyehue deformation

3.2.1 *Ring fractures*

In addition to pit crater formation on the forced fold, high spatial resolution satellite imagery (<3 $m\,px^{-1}$) also illustrates the progression of visible deformation occurring within Puyehue caldera from 2012 onward (Figure 8). The abundance of ring fractures encircling the center of the caldera visible in the most recent satellite imagery served as the initial indicator of caldera deformation. To better understand the timing of this deformation (since no mention of ring fractures inside Puyehue caldera could be found from any other source), we looked at historical imagery to determine whether these ring fractures are indeed a new feature or something that had been overlooked. Going back to April 2012, the earliest relatively snow free high-resolution satellite image of the caldera available to us, we see no evidence of any ring fractures within the caldera (Figure 8A) which indicates that the formation of ring fractures is indeed a recent phenomenon and began sometime after the end of the 2011–2012 Cordón Caulle eruption. Analyzing the entire collection of satellite imagery at our disposal, the first evidence of ring fractures does not show up until January 2017, with thin fracture lines appearing ~400 m to the west and north of the caldera center. By April 2019 (no snow free image was available in 2018), the original fractures seen in 2017 had grown to fully formed ring fractures around the center of the caldera. A year later in April 2020, no new fractures are visible but existing ring fractures had clearly continued to grow. The outermost fractures increased in length, while nearly all fractures appeared to become wider and deeper. Additionally, notable deformation in the very center of the caldera had occurred, as it looked markedly different than in previous images (prior to 2020). The subsequent image from April 2023 shows the continued growth of existing ring fractures (widening and deepening) as well as the formation of two new fractures towards the northeast rim of the caldera. Finally, a high-resolution SAR image (0.5 $m\,px^{-1}$) from April 2024 offers the most current snow-free satellite image of ring fractures and shows evidence of even more new fractures developing towards the very center of the caldera.

3.2.2 *Puyehue pit craters*

Beyond the formation of ring fractures, optical satellite imagery also reveals the formation of pit craters within Puyehue caldera. Evidence of pit craters dates back to our earliest image from April 2012, where two possible pits can be found towards the outer regions of the caldera (Figure 9). Satellite images show that new pit craters formed sometime between 2012 to 2015, predating any signs of ring fractures or measured deformation from DEMs. By 2019, a number of new pit craters had formed in the western part of the caldera near the outermost ring fractures. While in the most recent optical image from March 2024, even more pit craters are visible towards the very outer parts of the caldera, some forming pit chains that look like the early stages of new ring fractures. The formation of pit craters and pit crater chains within the caldera possibly signals the draining of material into the subsurface (as there is no evidence from the satellite imagery that these are explosion pits). Their coeval formation with fractures implies the existence of extensional stresses towards the outer portions of the caldera, leading to similar conditions responsible for pit crater formation observed on the Cordón Caulle forced fold following the 2011–2012 eruption.

3.2.3 *Puyehue caldera subsidence measured from DEMs*

Based on the timing of ring fracture formation determined using satellite imagery, we expected that caldera subsidence should be measurable beginning sometime around 2017 and continuing onward into 2024. The available DEMs within our collection corresponding closest to this period are from 2016, 2019 and 2024. Analysis of elevation profiles taken across the entire diameter of the caldera using DEMs from these three years (in addition to DEMs from 2011 and 2013 to help establish a baseline) shows that caldera deformation is marked by a significant amount of subsidence that has occurred from 2016 until 2024 at a variable rate (Figure 10). From 2016 to 2019 we measure nearly 23 m of subsidence, resulting in a subsidence rate of approximately 7.7 $m\,yr^{-1}$ (assuming a constant rate). Comparatively, we only measure about 12 m of subsidence from 2019–2025, which results in a much slower rate of 2.4 $m\,yr^{-1}$. In total, our elevation profiles show that the center of the caldera has subsided ~35 m from 2016 to 2024. Additionally, the profiles illustrate that subsidence is forming

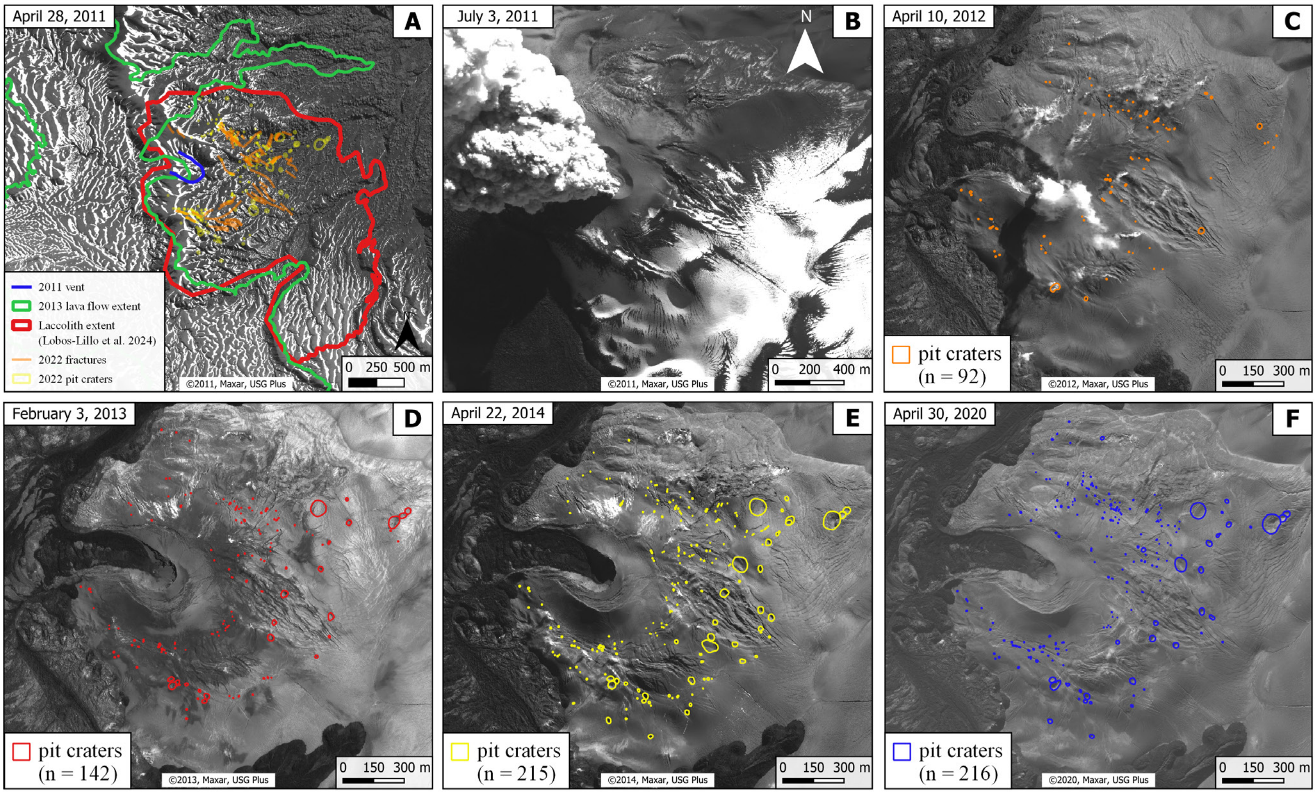

Figure 6: Time series of 2011–2012 Cordón Caulle eruption and subsequent pit crater formation from WorldView satellite images. [A] Pre-eruption image with the location of the 2011 vent along with the extent of the shallow intrusion and lava flow plotted for reference. The locations of pit craters and fractures mapped using the 2022 drone image are also plotted to show that these are not pre-eruptive features. [B] 1-month after the beginning of the eruption period. Large ash plumes were still erupting from the two visible vents while large fractures can be seen directly to the east of the vents. No pit craters are visible in this image, but the change in topography caused by shallow intrusion emplacement and erupted lava is clearly noticeable. [C] The first evidence of pit craters on the forced fold above the shallow intrusion is in April 2012, with a total of 92 pit craters able to be mapped. Pit craters are distributed in a horseshoe shape around the now singular vent feature. Many more fractures can also be found to the south and north of the vent. Steam emanating from the vent and from multiple fractures is also visible. [D–E] Continual pit crater formation and fracture growth can be seen over the following 2-year period from 2012–2014. Processes related to shallow intrusion emplacement were still actively shaping the environment years after the official end of the eruption period. Steam coming from fractures and pit crater chains indicates that the shallow intrusion was still very hot. [F] From 2014–2020 we see a sharp drop off in pit crater formation, indicating a majority of the pit craters which currently exist likely formed by April 2014. There are 216 pit craters mapped in 2020 at 0.5 m pixel^{-1} compared to the 349 mapped in Figure 3 from the 2022 drone image with higher spatial resolution.

a conical shaped depression that is approximately 400 m in diameter towards the center of the caldera, while more distal regions towards the edges of the caldera don't appear to be subsiding in any significant way.

4 Discussion

4.1 Cordón Caulle pit crater formation mechanism

Pit crater formation following the 2011–2012 Cordón Caulle eruption occurred over the entire forced fold area alongside the formation of extension fractures, normal faults and graben. The syn-eruptive shallow intrusion (<1 km depth) resulted in nearly 200 m of uplift during the first month of the eruption [Castro et al. 2016] and the resulting forced fold had areas of extension at the surface and above the lateral intrusion edge [Magee 2024], consistent with the numerous normal faults observed (Figure 6). The uplift was directly followed by post-eruptive subsidence that was caused by several processes at various scales that could have created void space and collapse in the forced fold (e.g. cooling, crystallization, lateral movement, compaction, melting of snow, and degassing) [Lillo et al. 2024]. The surface material across the forced fold largely consists of tephra deposits up to tens of meters in thickness from the multiple explosive phases that occurred throughout the 9-month long eruption period [Bonadonna et al. 2015; Lillo et al. 2024]. We interpret the mechanism of Cordón Caulle pit crater formation as the drainage of unconsolidated surface material (mostly tephra layers) into subterranean void space created by the dilation of normal faults, extension fractures, and the mechanisms driving subsidence. Pits we encountered in the 2025 field season and photographed in previous field seasons all display characteristics consistent with collapse pits instead

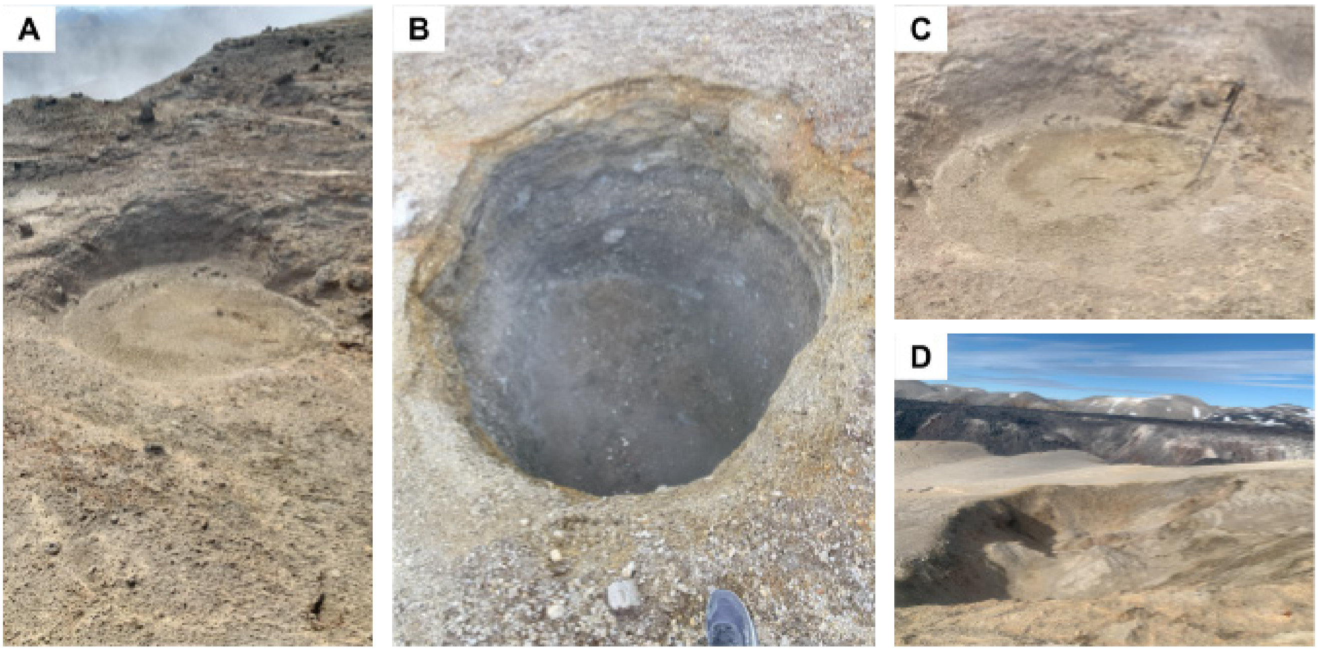

Figure 7: Field photos from January 2025 highlighting the different morphologies of PCC pit craters (see Supplementary Material 1 Figure S3 for locations of photos). [A] Small and shallow pit (~1.5 m in diameter and ~20 cm deep) with a nearly flat bottom. [B] Cylindrical pit (~1 m in diameter) that is nearly circular in plan-view. Multiple different tephra layers are visible in pit walls. [C] Shallow pit observed slightly south of the vent. Note that nearly half the walking pole in the image is underground. For many of the small and shallow pits we encountered in the field, the pit bottoms are quite soft. [D] Large and deep conical shaped pit (~40 m in diameter) that has a non-circular shape in plan-view. No visible layering in the pit walls.

of an over-pressurized fluid causing an explosion. A few pits we came across occurred in known bomb fields consisting of material ejected from the main vent during explosive phases of the eruption period; however, we found no field evidence suggesting that bombs proximal to these pits originated from pit craters themselves or that the bombs were responsible for forming pit craters (as there was no evidence of sag structures or impact craters at the scale of pit craters).

Additionally, more than 30 small and very shallow pits were observed in the field that are not able to be mapped using the drone data (see Figure 7 for photos and Supplementary Material 1 Figure S3 for locations of pits). We interpret these shallow pits as possible examples of younger pits still in the early stage of formation, where overlying material is slowly draining into subsurface void spaces as it is made available. We also acknowledge that this facet of our study would benefit from future work to map all the small and shallow pits that are not mapped from our 2022 drone image. The number of these pits mapped during our 2025 field campaign suggests a large number of these unmapped pits exist along the upper part of the forced fold and are likely associated with buried faults.

Our analysis of the relationship between pit craters and pit crater chains compared to faults and fractures also points towards pits on the forced fold as collapse pits. Figure 5 shows that the overall elongation of all pit craters only roughly tends to be aligned with the dominant orientation of faults and fractures. However, when looking only at pits that make up well defined pit chains, the alignment between elongated pit craters and fractures becomes much clearer and tends to follow a NW–SE direction. Pits formed due to faulting are expected to be elongated parallel to the strike angle of the fault responsible for pit formation [Ferrill et al. 2004; Magee et al. 2022]. We find this holds true mainly for pits forming pit crater chains, which are often found bounded by normal faults (see Figure 11 for example of pit crater elongated in direction of bounding faults).

4.2 Cordón Caulle pit crater timing and evolution

Post-eruption imagery revealed that pit craters did not form all at once, but over the course of at least three years from 2011 to 2014 (Figure 6). The window of snow free images at PCC being limited to a relatively short 2–3 month period every year meant that the effective temporal resolution of our imagery was about one usable image per year. The first evidence of pit craters is in April 2012 but must have occurred earlier. The onset of pit crater formation in 2012 aligns temporally with the beginning of subsidence on the shallow intrusion and the high frequency of pit crater formation from 2012–2014 is consistent with the period with the highest subsidence rate post-eruption [Lillo et al. 2024]. Early pits were mainly small to medium sized and were spread out all across the forced fold with no clear spatio-temporal patterns dictating pit formation. While we note there is SAR imagery that exists between the optical images from July 2011 and April 2012 (see Table S1 in Delgado et al. [2019]), we are not confident that pit craters would be visible in the SAR imagery ($3\ \mathrm{m\,px^{-1}}$) prior to the optical imagery ($0.5\ \mathrm{m\,px^{-1}}$) due to

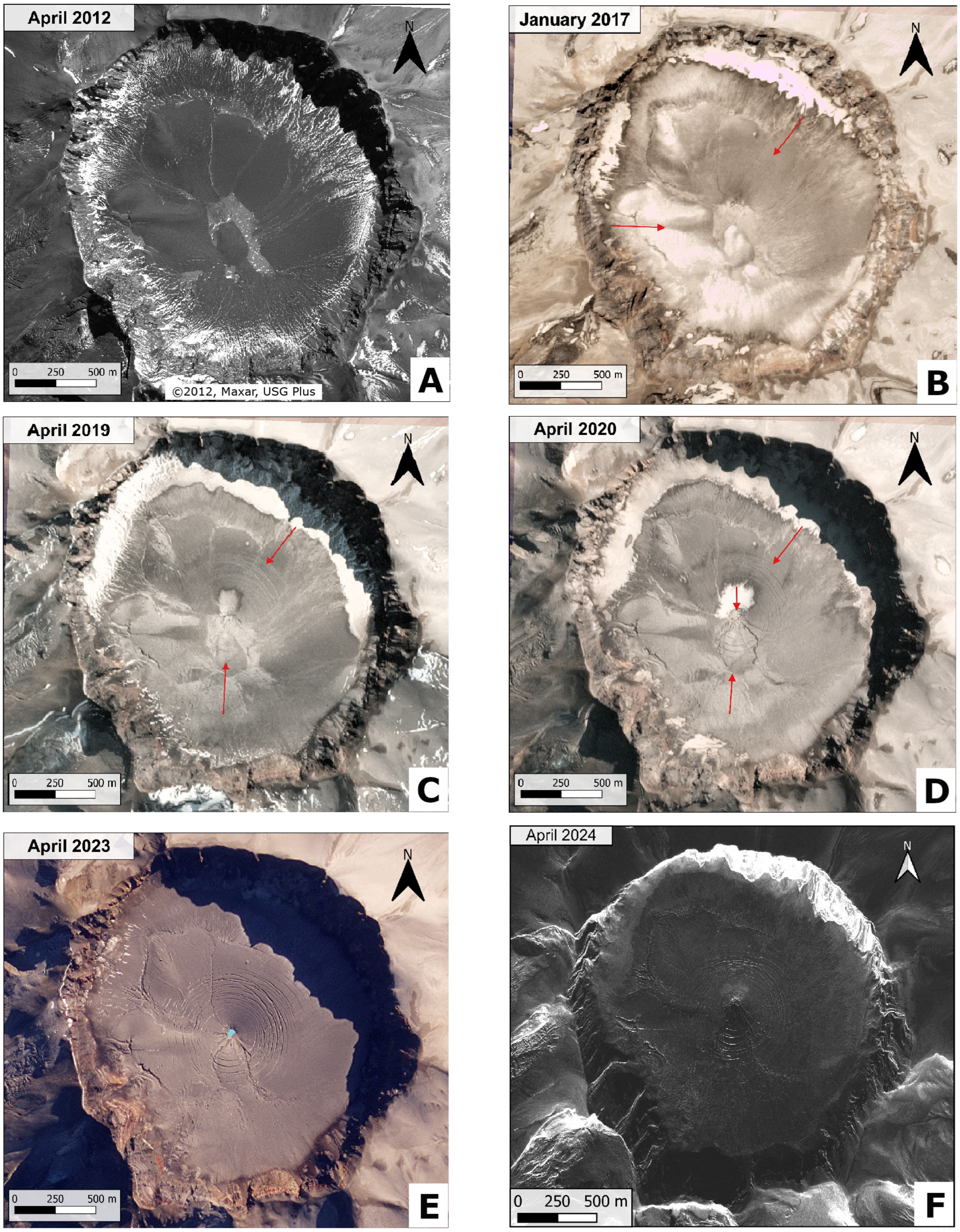

Figure 8: Time series of Puyehue caldera (see Figure 2 for location) from satellite imagery documenting formation and growth of ring fractures. [A] WorldView-2 optical image from the end of the 2011–2012 Cordón Caulle eruption period showing no signs of deformation inside the caldera. [B–E] PlanetScope multispectral images from 2017–2023. The first visible evidence of fractures developing within the caldera shows up beginning in January 2017. Over the next several years, continual fracture growth forms concentric ring faults around the center of the caldera. The formation of new ring fractures over time tends to migrate from the outer portions of the caldera towards the center, which is also where we measure the greatest amount of subsidence. [F] Capella SAR image showing the most current snow free image of the entire caldera. New ring fractures since 2023 can be seen around the very center illustrating ongoing deformation.

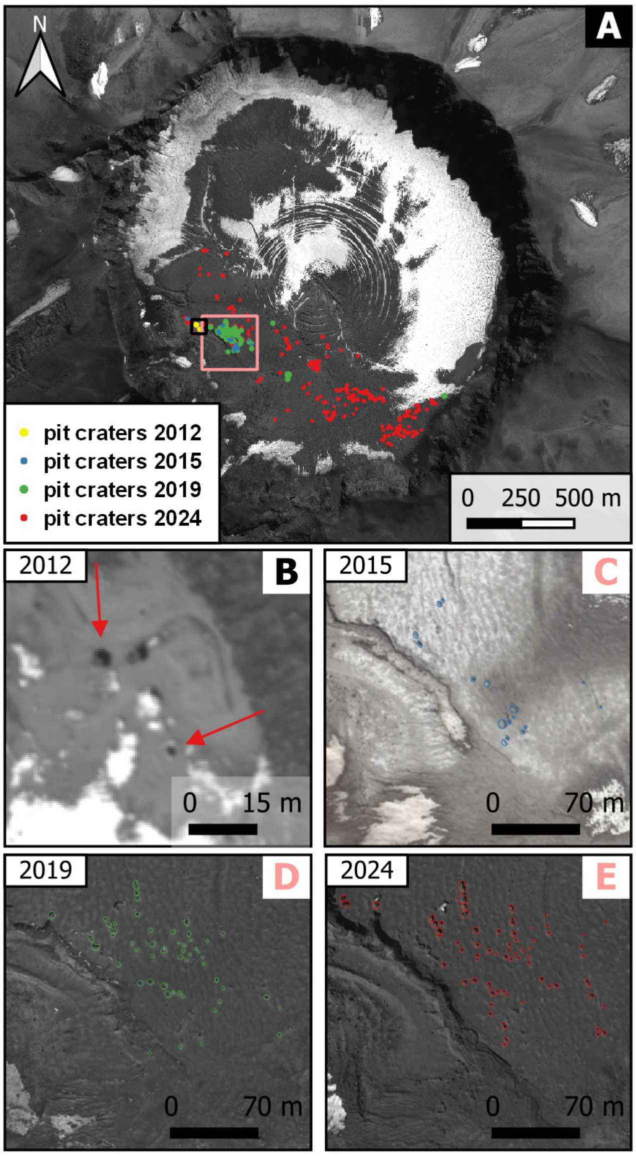

Figure 9: Time series of pit crater formation within Puyehue caldera documented from high resolution optical satellite imagery. First possible pit craters are seen as early as 2012 (earliest available optical image) with a few new pit craters forming by 2015 (we note that the 2015 WorldView image was not part of the data in our collection and therefore was only able to be viewed using Google Earth Pro). By 2019 and 2024, we observe significant pit crater formation along the outer eastern to southwestern portions which also coincides with the onset of subsidence and ring fracture formation.

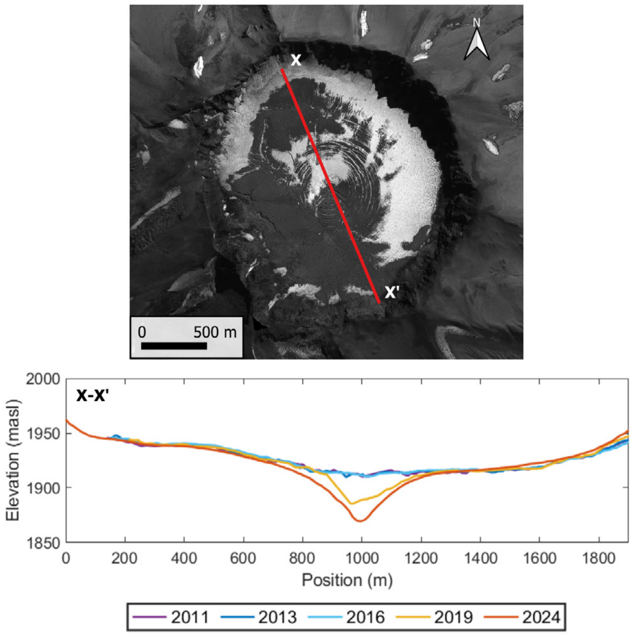

Figure 10: Elevation profiles along Puyehue caldera with DEMs from 2011, 2013, 2016, 2019 and 2024. Profile along X–X' cross section is plotted on top of Pléiades panchromatic optical image from March 29, 2024 in red. Profiles show no signal of deformation from 2011–2016 followed by nearly 35 m of subsidence at the caldera center over the next 8 years from 2016–2024.

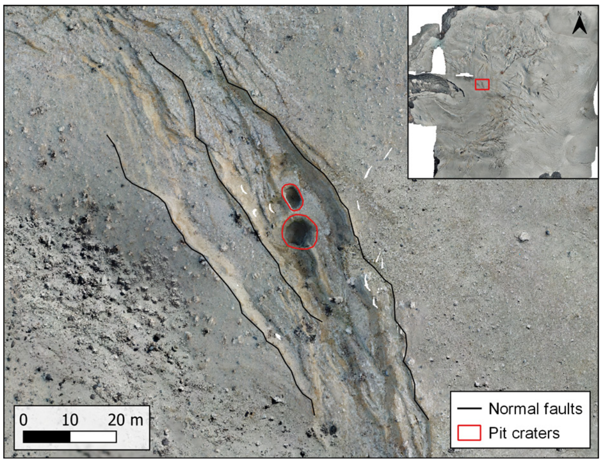

Figure 11: Pit crater formation within graben slightly east of the vent via 2022 drone image. Black lines are normal faults defining the sides of the graben while red lines outline pit craters. Note that the oval shaped pit is elongated in the same direction as fault orientation (NW–SE).

the difference in spatial resolution. As seen from comparing the number of pits mapped using the 2020 satellite image (n = 216) compared to using our 2022 drone image (n = 349), just going from a resolution 10 cm px^{-1} to 50 cm px^{-1} results in around 30 % less visible pit craters.

In addition to understanding the timing of pit crater formation, we also sought to understand the temporal evolution of pit crater and pit crater chain morphology. Starting with pit crater chains, we focused primarily on the north part of the forced fold, as the dense formation of pit chains here proved to be a great sandbox to document their evolution. Figure 12 shows a time series from our optical imagery documenting the evolution of multiple pit craters chains in this area. The earliest image, shows that many pit chains begin as assemblages

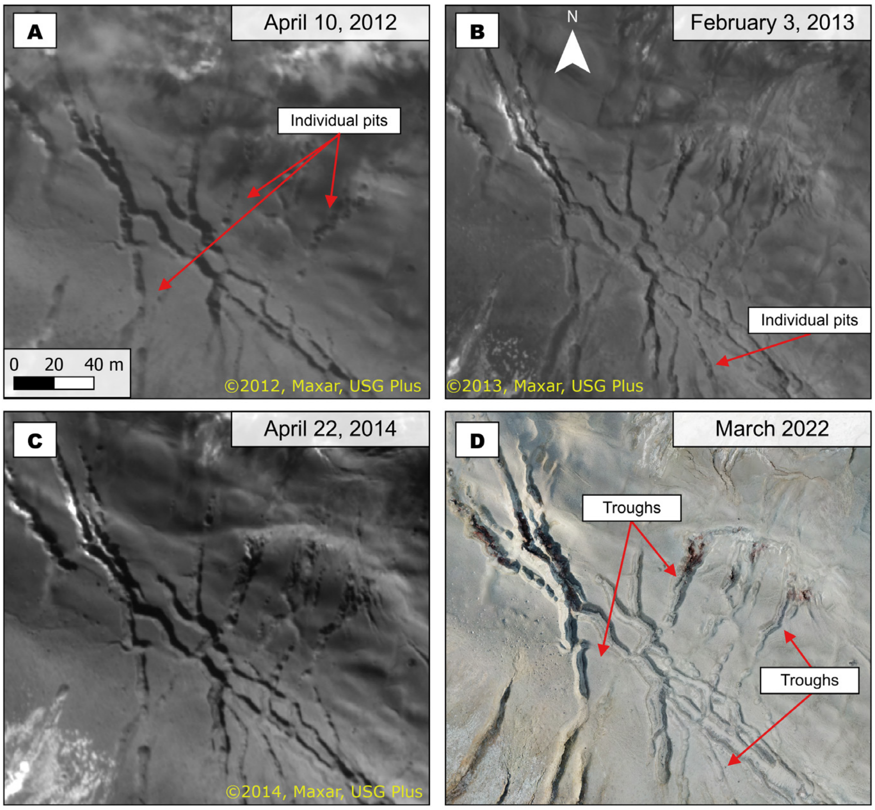

Figure 12: Time series from WorldView and drone imagery showing the evolution of pit crater chains on the forced fold from collections of individual pits to continuous trough-like features (see Supplementary Material 1 Figure S3 for location of pit chains). [A] Starting in April 2012, pit chains are clearly made up of individual pits in close proximity to each other. [B] Individual pits forming early pit chains have begun to coalesce and new pit crater chains have formed. [C] Existing pit crater chains have evolved into continuous features with less evidence of individual pits. [D] Most pit crater chains have fully evolved into features resembling troughs with no evidence of individual pit craters.

of individual pits that do not overlap, but still form a linear pattern. Over the course of almost a year, individual pits begin to coalesce giving pit chain formations a more continuous structure rather than a linear pattern of discrete or individual pits. The evolution away from individual pits continues further into the final satellite image, though evidence of individual pits still exists at this date. Finally, in our drone image, evidence of individual pits is almost all but gone, giving rise to the smooth trough-like features that currently appear all across the forced fold. Understanding how several of these pit chains have evolved over time suggests that many of the other similar structures resembling troughs in this region are in fact pit crater chains (in the latter stage of their evolution) despite the lack of evidence of individual pits. Many of these possible pit chain structures also have light-colored bottoms (same color as surface) with darker colored walls, which is the same way nearby pits appear. As a result, we find that these trough-like features are the end result of individual pits that eventually coalesced over time due to either continual drainage of material enlarging existing pits, or from erosional processes widening pits until they eventually joined together.

4.3 Pit crater morphology and field observations

Pit crater morphology is diverse, with anything between small, shallow cylindrical pits to large, deep conical shaped pits showing up. Large pits, in addition to pits to the north and directly east of the vent, all tend to have an inverted conical shape. The smooth walls and fine-grained deposits at the bottom of these pits is suggestive of formation in material with very low mechanical strength (i.e. fine grained tephra). Satellite imagery shows that many of these pits began as conical pits, with some of the larger pits developing flat bottoms from material deposited by fluvial systems. On the other hand, smaller pits to the south of the vent are more cylindrical shaped, appearing to have rougher walls and forming in more consolidated material. Since many of these pits are small, it is difficult to determine whether these pits formed with a cylindrical shape due to the resolution of satellite imagery not providing enough detail. Regardless, the correlation between cylindrical pits occurring in more consolidated material suggests that the increased material strength gives these pits the ability to resist weathering and maintain their shape. We therefore gather that the mechanical strength of the material is the main factor which influences the initial shape and evolution of pit crater morphology, with cylindrical pits tending to form in higher strength material. To further extend the usefulness of these findings, an area of future of work at Cordón Caulle could be to use pit crater morphology to help inform any variations in the layering and mechanical strength of the overlying material above the shallow intrusion, following similar methodologies to work done by de Luis and Parro [2025] studying pit craters on asteroids and small planetary bodies.

4.4 Puyehue caldera deformation

4.4.1 *Ring fracture and pit crater formation*

Following the 2011–2012 Cordón Caulle eruption, no physical signs of ring fractures within Puyehue caldera are apparent until January 2017, when the first fractures started to form (Figure 8). The continual growth of early fractures into ring fractures, the steady formation of new fractures in subsequent years, and the subsidence measured by DEMs between 2016, 2019, and 2024 shows that deformation has been an ongoing process not occurring in a single event. Comparing the evolution of ring fractures from year to year shows a somewhat steady growth of fractures and a trend of more pronounced deformation towards the center of the caldera, which is consistent with where the greatest amount of subsidence was measured in the elevation profiles.

A surprising result was the discovery of pit crater and pit crater chain formations within the caldera alongside ring fractures (Figure 9). Through including imagery available in Google Earth Pro, we find that pit crater formation began at least by February 2015, prior to any physical sign of fractures or measurable subsidence from any elevation profiles. Additionally, the formation of pit crater chains alongside fractures and the lack of evidence in the satellite imagery for pit craters having raised rims or surrounding ejecta suggests that these are also collapse pits similar to the pit craters on the forced fold. We note that pit craters only seem to be forming within the western and southern parts of the caldera for unknown reasons—possibly they are easier to form or detect in that region because of the material there. We speculate that more pit craters could form in that area if the removal of buried snow is the cause of the collapse. There was likely significant snow in Puyheue caldera (more than 2 meters based on comparing DEMs in February and March 2024 [Olitt 2025]) beneath the tens of centimeters to meter of tephra deposited during the 2011–2012 eruption in that location [Pistolesi et al. 2015]. The snow in the southwestern corner of Puyehue caldera is observed to melt earlier in the season [Olitt 2025] because it receives more sunlight than other portions of the caldera and this could lead to melting of the subsurface ice in that location, possibly facilitated by the fracturing induced by caldera subsidence.

4.4.2 *Caldera subsidence*

The elevation profiles show that non-uniform subsidence has caused the morphology of the caldera to change by forming an inverted conical or funnel shaped feature in the center (Figure 10). Experimental studies of caldera formation by Roche et al. [2000] has shown that funnel calderas can form as a result of collapse into small, deep magma chambers. Therefore, subsidence may be consistent with 2011 co-eruptive magma withdrawal from a reservoir beneath Puyehue determined to be at ~6 km depth by Jay et al. [2014]. However, in other studies of caldera deformation, subsidence or uplift that is not co-eruptive is usually seen within days to months of a change in volume or pressure inside the underlying magma reservoir [Cole et al. 2005]. Thus, if Puyehue subsidence is indeed related to the 2011–2012 eruption, then it is straying quite far from typical response timing. So much so that there is no documented evidence of caldera deformation lagging behind a change in subsurface magma storage conditions by nearly six years (or three years if we consider the formation of pit craters).

Could the subsidence at Puyehue be related to the >1 m of post-eruptive inflation of the magma reservoir at Cordón Caulle [Delgado et al. 2016; Delgado 2021] instead of the 2011 co-eruptive subsidence? Inflation could be caused by episodic recharge from a laterally connected magmatic source beneath the PCC complex [Delgado 2021] or other mechanisms like poroelastic behavior of a mushy reservoir [Phelps et al. 2023]. Perhaps the inflation observed with InSAR at Cordón Caulle after 2016 is fed by magma withdrawal from Puyehue that triggered the formation of fractures in the caldera. Although magma withdrawal at Puyehue has not been measured yet using InSAR, the timing would align much better with the onset of caldera fractures we observed from satellite images. In any case, we believe there is still not enough information to clearly decide what the catalyst for the current Puyehue caldera subsidence is and it invites further exploration in the future.

5 Conclusions

Combining the analysis of drone and satellite remote sensing datasets with in-situ field work observations, we present a comprehensive look into pit crater formation within the PCC volcanic complex following the 2011–2012 Cordón Caulle eruption. Field observations from multiple field seasons at Cordón Caulle confirm that pit craters mapped from high spatial resolution remote sensing imagery lack raised rims and surrounding ejecta, indicating that Cordón Caulle pit craters indeed formed through collapse rather than from an explosive mechanism. The causes of collapse include dilational faulting and extension fracturing caused by the extreme extensional stresses the region experienced following syn-eruptive shallow intrusion emplacement and subsequent subsidence as well as melting of snow buried by the newly erupted thick layers of tephra. The subsurface collapse occurring in primarily unconsolidated material was the mechanism leading to extensive pit crater and pit crater chain formation. Additionally, the consistent formation of pit crater chains aligned with normal faults and within graben on the shallow intrusion support dilational faulting as the dominant mechanism controlling pit crater formation.

At Puyehue volcano, we document for the first time >35 m of caldera subsidence from 2016–2024 and deformation in the form of ring fractures and pit crater formation. Analysis of optical satellite imagery shows that pit crater formation began by 2015 and predates evidence of fracture formation which is not visible until 2017. In either case, the first signs of deformation are temporally offset from the 2011–2012 Cordón Caulle eruption suggesting that the source processes responsible for deformation may be unrelated and indicative of new activity. Our analysis of DEMs from post-2011 show that Puyehue caldera has subsided at a decreasing rate of several meters per year and has formed a funnel-shape depression at its center. While this is helpful to understand the broad evolution of subsidence at Puyehue caldera, more precise estimates of deformation may require incorporating different datasets and analysis tools (e.g. InSAR). Ultimately, we attribute subsidence as the responsible mechanism creating extensional stresses within Puyehue caldera leading to fracture and pit crater formation. However, the source of subsidence remains unclear and is worth continued study in the future to uncover why deformation is occurring and to assess any possible future hazard.

In addition to determining the mechanism of PCC pit crater formation, we also clearly document real time pit crater formation and evolution using high resolution satellite remote sensing imagery. Active pit forming events occurring on Earth are infrequent, but there are now several examples including PCC that provide insight into how pit craters in similar geologic environments may have formed in the past on other planetary bodies. Here, we tracked individual pits as well as pit crater chains to understand how they evolve through their life cycle. In many cases, we found that troughs and pit crater chains are a latter part of the evolutionary processes of individual pit craters which formed in very close proximity. The earliest pit crater chains observable in our satellite imagery show evidence that many of these features start out as multiple individual pits which do not overlap. Over time, individual pits which makeup pit chains begin to coalesce (either from additional collapse or erosional processes) to form many of the continuous trough-like features we see today. Importantly, this may also help us understand the relative age of these features on other planetary bodies by assessing whether pit crater chain morphology resembles assemblages of individual pits or troughs.

Author Contributions

Alonzo Olitt: Data collection, analysis, and interpretation, Drafting the article; Diego Lobos-Lillo: Data collection and interpretation, Drafting the article; Matthew Pritchard: Data interpretation, Drafting the article; Carolina Muñoz-Saez: Data collection and interpretation, Critical revision of the article; Patrick Phelps: Data collection, Critical revision of the article; Philipp Ruprecht: Data collection, Critical revision of the article.

Acknowledgements

This work was supported by the National Science Foundation through proposal EAR-2317730 and by the NASA Science Mission Directorate project 80NSSC21K0842. Planet, Capella, and Vantor data were made available through NASA's Commercial SmallSat Data Acquisition (CSDA) Program. We also thank the Committee on Earth Observation Satellites (CEOS) Global Volcano Early Warning and Eruption Response from Space (G-VEWERS), Airbus, and Centre National d'études spatiales (CNES) for Pléiades data. The field photo of Puyehue caldera included in the supplemental material was kindly provided by Matías Calvert Mellado, a Geology undergraduate student at the Universidad Austral de Chile. We thank Craig Magee and an anonymous reviewer for critical comments that improved the manuscript. We also thank Craig Magee for sharing the data he collected in Fig. 11 of Magee et al. [2022].

Data Availability

All shapefiles produced in this study mapping pit craters, pit crater chains, faults and fractures at PCC from remote sensing imagery have been made openly available via the Zenodo repository linked here: https://zenodo.org/doi/10.5281/zenodo.15645911. The drone data, new 2024 Pléiades DEM, and complete database of Cordón Caulle pit crater morphometric properties from drone based measurements is also included in this repository.

Copyright Notice

References

Aron, F., P. Ruprecht, N. Vera, and F. Delgado (2025). "Syn-eruptive surface faulting reveals laccolith deformation dynamics at the 2011-2012 Cordón Caulle, Chile eruption". *AGU Fall Meeting Abstracts*. Volume 2025. AGU Fall Meeting Abstracts, V51D-0063, pages V51D–0063.

Bersson, J. J., A. B. Clarke, and J. R. Arrowsmith (2026). "Secondary explosions on silicic lavas: A case study from Banco Bonito rhyolite lava flow, New Mexico". *Journal of Volcanology and Geothermal Research* 472, page 108569. doi: 10.1016/j.jvolgeores.2026.108569.

Björnsdóttir, Þ. and P. Einarsson (2013). "Evidence of recent fault movements in the Tungnafellsjökull fissure swarm in the Central Volcanic Zone, Iceland". *Jökull* 63(1), pages 17–32. doi: 10.33799/jokull2013.63.017.

Bonadonna, C., M. Pistolesi, R. Cioni, W. Degruyter, M. Elissondo, and V. Baumann (2015). "Dynamics of wind-affected volcanic plumes: The example of the 2011 Cordón Caulle eruption, Chile". *Journal of Geophysical Research: Solid Earth* 120(4), pages 2242–2261. doi: 10.1002/2014JB011478.

Bufféral, S., E. Panza, S. Mannini, Á. R. Hjartardóttir, A. Nobile, N. Gies, B. V. Óskarsson, and J. Ruch (2023). "Surface fractures generated during the 2021 Reykjanes oblique rifting event (SW Iceland)". *Bulletin of Volcanology* 85(11). doi: 10.1007/s00445-023-01666-9.

Castro, J. M., B. Cordonnier, C. I. Schipper, H. Tuffen, T. S. Baumann, and Y. Feisel (2016). "Rapid laccolith intrusion driven by explosive volcanic eruption". *Nature Communications* 7(1), page 13585. doi: 10.1038/ncomms13585.

Clifton, A. and P. Einarsson (2005). "Styles of surface rupture accompanying the June 17 and 21, 2000 earthquakes in the South Iceland Seismic Zone". *Tectonophysics* 396(3-4), pages 141–159. doi: 10.1016/j.tecto.2004.11.007.

Cole, J., D. Milner, and K. Spinks (2005). "Calderas and caldera structures: a review". *Earth-Science Reviews* 69(1-2), pages 1–26. DOI: 10.1016/j.earscirev.2004.06.004.

Crumpler, L. and J. Aubele (1978). "Structural evolution of Arsia Mons, Pavonis Mons, and Ascreus Mons: Tharsis region of Mars". *Icarus* 34(3), pages 496–511. DOI: 10.1016/0019-1035(78)90041-6.

De Crescenzo, L., E. Christiansen, and J. Radebaugh (2022). "The Origin of Lava Pits—Inflation or Collapse? Constraints from Lidar and drones at Black Butte, Idaho". *53rd Lunar and Planetary Science Conference*. Volume 2678, page 2944.

De Natale, G., S. M. Petrazzuoli, and F. Pingue (1997). "The effect of collapse structures on ground deformations in calderas". *Geophysical Research Letters* 24(13), pages 1555–1558. DOI: 10.1029/97GL01600.

Delgado, F. (2021). "Rhyolitic volcano dynamics in the Southern Andes: Contributions from 17 years of InSAR observations at Cordón Caulle volcano from 2003 to 2020". *Journal of South American Earth Sciences* 106, page 102841. DOI: 10.1016/j.jsames.2020.102841.

Delgado, F., J. Kubanek, K. Anderson, P. Lundgren, and M. Pritchard (2019). "Physicochemical models of effusive rhyolitic eruptions constrained with InSAR and DEM data: A case study of the 2011-2012 Cordón Caulle eruption". *Earth and Planetary Science Letters* 524, page 115736. DOI: 10.1016/j.epsl.2019.115736.

Delgado, F., M. E. Pritchard, D. Basualto, J. Lazo, L. Córdova, and L. E. Lara (2016). "Rapid reinflation following the 2011–2012 rhyodacite eruption at Cordón Caulle volcano (Southern Andes) imaged by InSAR: Evidence for magma reservoir refill". *Geophysical Research Letters* 43(18), pages 9552–9562. DOI: 10.1002/2016GL070066.

De Luis, M. and L. M. Parro (2025). "Analysis of pit craters on asteroids and small bodies: Predictions about the regolith layer and internal structure". *Icarus* 433, page 116514. DOI: 10.1016/j.icarus.2025.116514.

Ferrill, D. A., D. Y. Wyrick, A. P. Morris, D. W. Sims, and N. M. Franklin (2004). "Dilational fault slip and pit chain formation on Mars". *GSA Today* 14(10), page 4. DOI: 10.1130/1052-5173(2004)014%3C4:dfsapc%3E2.0.co;2.

Ferrill, D. A., D. Y. Wyrick, and K. J. Smart (2011). "Coseismic, dilational-fault and extension-fracture related pit chain formation in Iceland: Analog for pit chains on Mars". *Lithosphere* 3(2), pages 133–142. DOI: 10.1130/L123.1.

Frumkin, A. and R. Naor (2019). "Formation and modification of pit craters – example from the Golan volcanic plateau, southern Levant". *Zeitschrift für Geomorphologie* 62(3), pages 163–181. DOI: 10.1127/zfg/2019/0614.

Global Volcanism Program (2025). *Puyehue-Cordón Caulle*. Volcanoes of the World (v. 5.2.7; 21 Feb 2025). Distributed by Smithsonian Institution, compiled by Venzke, E. https://volcano.si.edu/volcano.cfm?vn=357150.

Gwinner, K., J. Head, J. Oberst, J. Gillis-Davis, Z. Xiao, R. Strom, F. Preusker, and S. Solomon (2012). "Morphology of pit craters on Mercury from stereo-derived topography and implications for pit crater formation". *43rd Annual Lunar and Planetary Science Conference*. 1659, page 1991.

Hardy, S. (2021). "Discrete element modelling of pit crater formation on Mars". *Geosciences* 11(7). DOI: 10.3390/geosciences11070268.

Head III, J. W. and L. Wilson (1993). "Lunar graben formation due to near-surface deformation accompanying dike emplacement". *Planetary and Space Science* 41(10), pages 719–727. DOI: 10.1016/0032-0633(93)90114-H.

Holohan, E. P., M. Schöpfer, and J. J. Walsh (2011). "Mechanical and geometric controls on the structural evolution of pit crater and caldera subsidence". *Journal of Geophysical Research: Solid Earth* 116(B7). DOI: 10.1029/2010JB008032.

Hughes, S. S., S. E. K. Nawotniak, D. W. Sears, C. Borg, W. B. Garry, E. H. Christiansen, C. W. Haberle, D. S. Lim, and J. L. Heldmann (2018). "Phreatic explosions during basaltic fissure eruptions: Kings Bowl lava field, Snake River Plain, USA". *Journal of Volcanology and Geothermal Research* 351, pages 89–104. DOI: 10.1016/j.jvolgeores.2018.01.001.

Hurley, M., N. Oestreicher, A. V. Shevchenko, G. P. De Pascale, M. T. Gudmundsson, E. Á. Gudnason, G. P. Hersir, B. F. De Jarnatt, A. Joachim, J. Ruch, F. L. Bonali, and T. R. Walter (2025). "Fracture dynamics and topographic controls at Mount Thorbjörn during the Svartsengi 2023–2024 volcanic unrest, Iceland". *Journal of Volcanology and Geothermal Research* 466, page 108407. DOI: 10.1016/j.jvolgeores.2025.108407.

Jay, J., F. Costa, M. Pritchard, L. Lara, B. Singer, and J. Herrin (2014). "Locating magma reservoirs using InSAR and petrology before and during the 2011–2012 Cordón Caulle silicic eruption". *Earth and Planetary Science Letters* 395, pages 254–266. DOI: 10.1016/j.epsl.2014.03.046.

Kling, C. and P. Byrne (2022). "Pit Crater Morphology is Not Unique to Setting or Formation". *53rd Lunar and Planetary Science Conference*. Volume 2678, page 2801.

Kling, C. L., P. K. Byrne, R. M. Atkins, and K. W. Wegmann (2021). "Tectonic Deformation and Volatile Loss in the Formation of Noctis Labyrinthus, Mars". *Journal of Geophysical Research: Planets* 126(11). DOI: 10.1029/2020je006555.

Kling, C. L. (2020). "Pit Craters Throughout the Solar System". PhD thesis. North Carolina State University.

Lillo, D. L., F. Delgado, M. Pritchard, P. Ruprecht, and C. Muñoz-Saez (2024). "Multiple sources of elevation change during and after the 2011–2012 Cordón Caulle, Chile eruption measured by satellite topographic time series". *Volcanica* 7(2), pages 541–564. DOI: 10.30909/vol.07.02.541564.

Magee, C. (2024). "Fractures and faults across intrusion-induced forced folds: a georesource perspective". *Geological Society, London, Special Publications* 547(1), pages 109–129. DOI: 10.1144/sp547-2023-47.

Magee, C., C. Kling, P. Byrne, and C. A-L Jackson (2022). "Seismic reflection data reveal the 3D subsurface structure of pit craters". *Journal of Geophysical Research: Planets* 127(8), e2021JE007155. DOI: 10.1029/2021JE007155.

Naranjo, J. A., B. Singer, B. Jicha, H. Moreno, and L. Lara (2017). "Holocene tephra succession of Puyehue-Cordón Caulle and Antillanca/Casablanca volcanic complexes, southern Andes (40–41 S)". *Journal of Volcanology and Geothermal Research* 332, pages 109–128. DOI: 10.1016/j.jvolgeores.2016.11.017.

Nuth, C. and A. Kääb (2011). "Co-registration and bias corrections of satellite elevation data sets for quantifying glacier thickness change". *The Cryosphere* 5(1), pages 271–290. DOI: 10.5194/tc-5-271-2011.

Okubo, C. H. and S. J. Martel (1998). "Pit crater formation on Kilauea volcano, Hawaii." *Journal of Volcanology and Geothermal Research* 86(1-4), pages 1–18. DOI: 10.1016/S0377-0273(98)00070-5.

Olitt, A. (2025). "Testing mechanisms of volcano crater formation at Puyehue-Cordón Caulle Chile with satellite, drone and field observations". Master's thesis. Cornell University.

Phelps, P. R., H. M. Gonnermann, H. Winslow, P. Ruprecht, M. E. Pritchard, F. Delgado, and Y. Liao (2023). "Feasibility of melt segregation from a crystal mush in response to the 2011–2012 eruption at Cordón Caulle, Chile". *Geophysical Journal International* 235(1), pages 610–634. DOI: 10.1093/gji/ggad259.

Pistolesi, M., R. Cioni, C. Bonadonna, M. Elissondo, V. Baumann, A. Bertagnini, L. Chiari, R. Gonzales, M. Rosi, and L. Francalanci (2015). "Complex dynamics of small-moderate volcanic events: The example of the 2011 rhyolitic Cordón Caulle eruption, Chile". *Bulletin of Volcanology* 77, pages 1–24. DOI: 10.1007/s00445-014-0898-3.

Poppe, S., E. P. Holohan, E. Pauwels, V. Cnudde, and M. Kervyn (2015). "Sinkholes, pit craters, and small calderas: analog models of depletion-induced collapse analyzed by computed X-ray microtomography". *GSA Bulletin* 127(1-2), pages 281–296. DOI: 10.1130/B30989.1.

Prockter, L., P. Thomas, M. Robinson, J. Joseph, A. Milne, B. Bussey, J. Veverka, and A. Cheng (2002). "Surface expressions of structural features on Eros". *Icarus* 155(1), pages 75–93. DOI: 10.1006/icar.2001.6770.

Pryce, E., J. Cartwright, C. Kirkham, and D. Phillips (2025). "Sequential phreatomagmatic eruptions during the lateral propagation of giant dyke swarms". *Geology* 53(3), pages 274–278. DOI: 10.1130/g52490.1.

Roche, O., T. H. Druitt, and O. Merle (2000). "Experimental study of caldera formation". *Journal of Geophysical Research: Solid Earth* 105(B1), pages 395–416. DOI: 10.1029/1999JB900298.

Schipper, C. I., J. M. Castro, H. Tuffen, M. R. James, and P. How (2013). "Shallow vent architecture during hybrid explosive–effusive activity at Cordón Caulle (Chile, 2011–12): evidence from direct observations and pyroclast textures". *Journal of Volcanology and Geothermal Research* 262, pages 25–37. DOI: 10.1016/j.jvolgeores.2013.06.005.

Scott, E. D., L. Wilson, and J. W. Head III (2002). "Emplacement of giant radial dikes in the northern Tharsis region of Mars". *Journal of Geophysical Research: Planets* 107(E4), pages 3–1. DOI: 10.1029/2000JE001431.

Scott, E. D. and L. Wilson (2002). "Plinian eruptions and passive collapse events as mechanisms of formation for Martian pit chain craters". *Journal of Geophysical Research: Planets* 107(E4). DOI: 10.1029/2000je001432.

Shevchenko, A. V., T. R. Walter, M. T. Gudmundsson, J. M. C. Belart, P. Marzban, E. U. Zorn, Þ. Sæmundsson, J. K. Helgason, J. M. Turowski, M. S. Vassileva, M. Motagh, and D. Müller (2024). "Morphological changes of the south-eastern wall of Askja caldera, Iceland over the past 80 years". *Communications Earth & Environment* 5(1). DOI: 10.1038/s43247-024-01616-z.

Shoemaker Thackston, E. S., D. M. H. Baker, J. A. Richardson, L. M. Carter, S. P. Scheidt, P. L. Whelley, and K. E. Young (2024). "Mapping Ice Buried by the 1875 and 1961 Tephra of Askja Volcano, Northern Iceland Using Ground-Penetrating Radar: Implications for Askja Caldera as a Geophysical Testbed for In Situ Resource Utilization". *Journal of Geophysical Research: Planets* 129(4). DOI: 10.1029/2023je007834.

Singer, B. S., B. R. Jicha, M. A. Harper, J. A. Naranjo, L. E. Lara, and H. Moreno-Roa (2008). "Eruptive history, geochronology, and magmatic evolution of the Puyehue-Cordón Caulle volcanic complex, Chile". *Geological Society of America Bulletin* 120(5-6), pages 599–618. DOI: 10.1130/B26276.1.

Smart, K. J., D. Y. Wyrick, and D. A. Ferrill (2011). "Discrete element modeling of Martian pit crater formation in response to extensional fracturing and dilational normal faulting". *Journal of Geophysical Research: Planets* 116(E4). DOI: 10.1029/2010JE003742.

Somoza, L., K. M. Andreassen, A. Plaza-Faverola, T. Medialdea, J. Gafeira, F. J. González, and G. R. Dickens (2025). "Giant pit craters on the modern seafloor above magma-induced hydrothermal vent complexes of Scotia Sea, offshore Antarctica". *Scientific Reports* 15(1). DOI: 10.1038/s41598-025-85899-y.

Veverka, J., P. Thomas, D. Simonelli, M. Belton, M. Carr, C. Chapman, M. Davies, R. Greeley, R. Greenberg, J. Head, et al. (1994). "Discovery of grooves on Gaspra". *Icarus* 107(1), pages 72–83. DOI: 10.1006/icar.1994.1007.

Whitten, J. L. and E. S. Martin (2019). "Icelandic pit chains as planetary analogs: Using morphologic measurements of pit chains to determine regolith thickness". *Journal of Geophysical Research: Planets* 124(11), pages 2983–2999. DOI: 10.1029/2019JE006099.

Wyrick, D., D. A. Ferrill, A. P. Morris, S. L. Colton, and D. W. Sims (2004). "Distribution, morphology, and origins of Martian pit crater chains". *Journal of Geophysical Research: Planets* 109(E6). DOI: 10.1029/2004JE002240.

Wyrick, D. Y. and K. J. Smart (2009). "Dike-induced deformation and Martian graben systems". *Journal of Volcanology and Geothermal Research* 185(1-2), pages 1–11. DOI: 10.1016/j.jvolgeores.2008.11.022.

Wyrick, D. and D. Buczkowski (2022). "Pit crater chains across the solar system: evidence for subterranean tectonic caves, porosity and permeability pathways on planetary bodies". *Journal of Geophysical Research: Planets* 127(12), e2022JE007281. DOI: 10.1029/2022JE007281.